Chinese Physics Letters

PAPER

# Rhombohedrally-Distorted Orthorhombic $Hf_{0.5}Zr_{0.5}O_{2-x}$ Stabilized by Cooperative Oxygen Vacancies and Lattice Distortions

To cite this article: Lei Liao *et al* 2026 *Chinese Phys. Lett.* **43** 030702

Chinese Physics Letters **43**, 030702 (2026)

# Rhombohedrally-Distorted Orthorhombic $Hf_{0.5}Zr_{0.5}O_{2-x}$ Stabilized by Cooperative Oxygen Vacancies and Lattice Distortions

Lei Liao(廖磊)[1,2,3†], Chen Zhang(张陈)[4†], Zhuohui Liu(刘倬卉)[1,3†], Chen Cai(蔡尘)[1,3],
Huacong Sun(孙华聪)[1,2,3], Xudan Huang(黄旭丹)[1,3], Ruijie Li(李瑞杰)[5], Wenxi Li(李文希)[1,5],
Dongbao Luo(罗东宝)[6], Jianlin Wang(王建林)[1,3], Xiao Li(李晓)[6], Lei Liu(刘磊)[5,7],
Kuijuan Jin(金奎娟)[1,3], Lifen Wang(王立芬)[1,3*], Huixiong Deng(邓惠雄)[4*],
Chen Ge(葛琛)[1,3*], and Xuedong Bai(白雪冬)[1,3*]

[1] *Beijing National Laboratory for Condensed Matter Physics and Institute of Physics,*
*Chinese Academy of Sciences, Beijing 100190, China*
[2] *SINOPEC Research Institute of Petroleum Processing Co., Ltd., Beijing 100083, China*
[3] *School of Physical Sciences, University of Chinese Academy of Sciences, Beijing 100049, China*
[4] *State Key Laboratory of Superlattices and Microstructures, Institute of Semiconductors,*
*Chinese Academy of Sciences, Beijing 100083, China*
[5] *School of Materials Science and Engineering, Peking University, Beijing 100871, China*
[6] *Center for Quantum Transport and Thermal Energy Science, Nanjing Normal University, Nanjing 210023, China*
[7] *Interdisciplinary Institute of Light-Element Quantum Materials and Research Center for Light-Element Advanced Materials, Peking University, Beijing 100871, China*

(Received 13 November 2025; accepted manuscript online 8 January 2026)

Hafnia-based ferroelectrics have emerged as promising materials for next-generation nanoelectronics owing to their robust nanoscale properties and compatibility with metal-oxide-semiconductor technology. However, their metastable nature remains a key challenge for practical implementation. Utilizing scanning transmission electron microscopy, we investigated the atomic-scale mechanisms governing ferroelectric transitions and the metastability of polar phases in 10-nm-thick $Hf_{0.5}Zr_{0.5}O_2$ thin films. Our results demonstrate that oxygen vacancies, coupled with rhombohedral distortions of the cation lattice, facilitate ferroelectric phase transitions and enable robust polar switching through adaptive processes, including cell-by-cell oxygen displacement and domain-wall-mediated nucleation and growth. These findings underscore the pivotal role of oxygen vacancies and lattice distortions in stabilizing polar phases and provide detailed insights into the atomic structures and transition dynamics of polymorphic $Hf_{0.5}Zr_{0.5}O_{2-x}$, thereby advancing its potential for practical device applications.

DOI: 10.1088/0256-307X/43/3/030702 CSTR: 32039.14.0256-307X.43.3.030702

Hafnia-based ferroelectric thin films have attracted significant research interest since the discovery of their unconventional ferroelectricity in 2011.[1] Unlike conventional perovskite ferroelectrics,[2–5] these materials exhibit robust ferroelectricity at the nanoscale and are compatible with complementary metal–oxide–semiconductor (CMOS) compatibility, making them promising candidates for next-generation low-power nonvolatile memories.[6,7] Despite extensive investigation, several fundamental questions remain unresolved, including the origin of ferroelectricity, phase transition mechanisms, ferroelectric fatigue, and the factors governing device performance. These challenges largely stem from the polymorphic nature of the fluorite-like material class. The thermodynamically stable phase of hafnium oxide ($HfO_2$) is the monoclinic phase (M phase, $P2_1/c$), which is non-ferroelectric. Among its polymorphs, the metastable orthorhombic (O phase, $Pca2_1$) and the rhombohedral phase (R phase, $R3m$) are widely regarded as the primary sources of ferroelectricity in $HfO_2$-based thin films.[8–11] The kinetic stability of these phases remains under active debate, governed by a complex interplay of extrinsic factors such as doping, strain, electrode interfaces, and oxygen vacancies.[12–17] Phase transitions between polar and non-polar structures play a critical role in ferroelectric activation and degradation; however, thermodynamic constraints impede the stabilization of metastable polar phases.[18–20] Consequently, the metastability of these polar phases, their ferroelectric switching behavior, and the underlying transition mechanisms remain elusive.

The polymorphic nature and nanoscale dimensions of hafnium-based ferroelectrics complicate high-precision structural analysis using conventional crystallographic characterization methods, such as X-ray diffraction and neutron scattering, which are typically optimized for bulk crystals.[21,22] Although scanning transmission electron

---

[†] These authors contributed equally to this work.

[*] Corresponding authors. Email: wanglf@iphy.ac.cn; hxdeng@semi.ac.cn; gechen@iphy.ac.cn; xdbai@iphy.ac.cn

microscopy (STEM) with high-angle annular dark-field (HAADF) imaging enables atomic-level identification of cation arrangements in oxides,[11] it provides limited information on oxygen positions owing to their lower scattering cross-section. Nevertheless, accurate determination of atomic positions in this complex binary system is crucial for understanding its unconventional polarization properties and associated phase transitions.[23] To overcome this challenge and achieve deeper insight into the lattice dynamics of hafnia-based ferroelectrics, we employed the recently developed differentiated differential phase contrast (dDPC)-STEM technique, which enables simultaneous visualization of both light and heavy elements at atomic resolution.[24–26] Compared with other light-element imaging methods,[26–32] dDPC-STEM has demonstrated superior precision in determining atomic positions.[33]

In this study, we investigate the polymorphic behavior and transition dynamics of 10-nm-thick $Hf_{0.5}Zr_{0.5}O_2$ (HZO) thin films, with particular emphasis on the metastable T- and O-phases and their stability relative to the thermodynamically stable M-phase. By employing dDPC-STEM imaging to determine the full atomic structure of the HZO thin films, we reveal a critical interplay between oxygen vacancy concentration and rhombohedral distortion of the cation lattice in the metastable phases. Specifically, T and O lattices containing oxygen vacancy concentrations of up to 4.7% exhibit rhombohedral distortion angles approaching 5°. *In situ* observations indicate that oxygen vacancies do not affect the polarization activation process during the transition from the nonpolar T-phase to the polar O-phase. However, they significantly enhance the stability of the distorted O phase while impeding the transition to the nonpolar M phase during ferroelectric switching.

We directly visualized the successive martensitic phase transitions from the T phase to the O phase and from the O phase to the M phase at atomic resolution in fully oxygen-stoichiometric HZO. In striking contrast, oxygen-deficient HZO exhibits a robust ferroelectric switching state characterized by adaptive mechanisms that integrate cell-by-cell oxygen displacement during the antiferroelectric transition with domain-wall-mediated nucleation and growth during polarization flipping in lattice-distorted O phases. This state appears kinetically trapped within oxygen-deficient regions. Supported by the density functional theory (DFT) calculations, charged oxygen vacancies are shown to stabilize the O phase. Our findings elucidate the atomic structure and dynamic evolution of polar HZO phases and their associated transitions, providing clear evidence for the coupled roles of oxygen vacancies and cationic lattice deformation in stabilizing the ferroelectric phase of hafnia-based films. These insights advance the fundamental understanding and technological development of hafnia-based ferroelectric devices.

*Atomic Structure of Rhombohedrally Distorted Orthorhombic-HZO.* Freestanding HZO thin films with a thickness of approximately 10 nm were synthesized using pulsed laser deposition,[34] followed by exfoliation and transfer onto a transmission electron microscopy (TEM) grid for plan-view imaging (Fig. S1 in Supplementary Materials). Energy-dispersive X-ray (EDX) mapping of the freestanding HZO samples demonstrates a uniform distribution of Hf and Zr, without detectable elemental segregation (Fig. S2). STEM imaging revealed that the synthesized HZO films consist of polycrystalline polymorphic nanograins, predominantly in the polar O-phase, consistent with previously reported HZO thin films.[35] As illustrated in Fig. 1(a), oxygen ions in O-phase HZO can be categorized into two types according to their displacements from the centers of the nearest Hf/Zr ion positions: threefold-coordinated off-center OI-type ions and fourfold-coordinated center-positioned OII-type ions. The polarization in HZO primarily arises from off-center displacements of 58 pm along the [001] crystallographic direction of the OI-type oxygen atoms, forming ferroelectric layers with a polarization vector of approximately 36 $\mu C/cm^2$, separated by non-polar OII-type layers within the O-phase HZO.

To examine the atomic structure and ferroelectric behavior of individual nanograins in HZO thin films, we employed aberration-corrected STEM equipped with HAADF imaging, segmented detectors for DPC imaging, and electron energy-loss spectroscopy (EELS). Atomic-resolution HAADF and dDPC images were obtained simultaneously, as schematically illustrated in Fig. 1(b). These micrographs reveal nanograins exhibiting lattice deviations from the ideal O-phase structure, where the vertical Hf/Zr lattice axis angle ($\alpha$) tilts from the 90° characteristic of the O-phase to a minimum of 85.5°, indicating a rhombohedral distortion (denoted $O_d$). This distortion is further illustrated in the lattice mapping shown in Fig. 1(c), where an angle map overlaid on the HAADF image highlights the spatial distribution of lattice deformation within O-phase nanograins of the HZO thin film. Additionally, the HZO films display polymorphic nanograins, comprising a small fraction of monoclinic (M-[111]), predominantly orthorhombic (O-[111], O-[001]), and minor amounts of tetragonal (T-[111], T-[100]) phases (see also Fig. S3).

The atomic structure of polar HZO deviating from the O-phase has previously been reported in epitaxially grown HZO as either the R phase[36] or the oIV ($Pmn2_1$) phase with a lattice angle $\alpha = 84°$,[37] as well as a polar monoclinic phase with an angle $\beta \approx 100°$,[38] configurations commonly attributed to epitaxial shear strain. In contrast, our investigation of 10-nm-thick HZO thin films reveals that intrinsic lattice deformation varies locally across nanograins, thereby ruling out a uniform residual epitaxial strain effect originating from the exfoliated substrate. Furthermore, EELS analysis of the $O_d$ phases, as shown in Fig. 1(d), suggests that the observed lattice deformation correlates with the presence of oxygen vacancies. The O $K$-edge energy-loss near-edge structure (ELNES) exhibits a characteristic double-peak profile, with peak A (∼534 eV) and peak B (∼537 eV) attributed to hybridization between the O 2p orbital and the Hf (or Zr) d-$e_g$ and d-$t_{2g}$ orbitals, respectively.[39,40] Previous studies have shown that the sharpness and relative intensity of peak A compared with peak B, as well as the energy position of peak B, vary with oxygen vacancy concentration in HZO

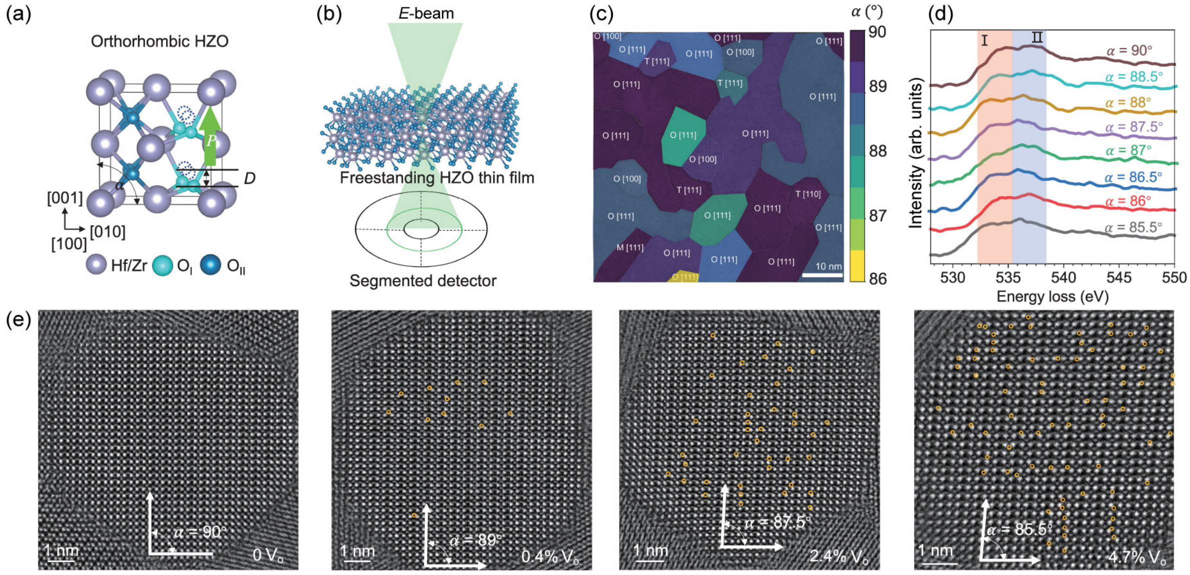

**Fig. 1.** Rhombohedrally distorted-orthorhombic $Hf_{0.5}Zr_{0.5}O_{2-x}$ ($0 \leq x \leq 0.094$) in 10-nm thick films. (a) Atomic structure model of the orthorhombic $Hf_{0.5}Zr_{0.5}O_2$ (HZO) unit cell; gray spheres represent Hf/Zr cations, blue spheres denote oxygen in unpolarized layers, and cyan spheres indicate oxygen atoms in polar layers. Off-center oxygen displacement ($D$) generates polarization within the unit cell. (b) Schematic illustration of the differential phase-contrast (DPC)-STEM configuration for real-space, atomic-resolution imaging of HZO thin films. (c) HAADF overview image of a freestanding HZO film displaying lattice distortion, with the lattice angle $\alpha$ mapped across individual nanograins. (d) O $K$-edge EELS spectra acquired from the distorted orthorhombic regions, indicating a reduced A/B peak intensity ratio and energy shifts in highly distorted nanograins. (e) dDPC images of distorted orthorhombic structures along the $[001]_o$ direction, with oxygen vacancy sites highlighted by dashed circles. Scale bar: 1 nm.

films.[41] In the highly distorted $O_d$ HZO, peak A is suppressed while peak B shifts toward lower energy, indicating an increased concentration of oxygen vacancies.

Simultaneous dDPC imaging further corroborates the presence of oxygen vacancies and identifies their precise locations within individual $O_d$ nanograins. Figure 1(e) shows representative dDPC images of O-phase grains oriented along the [100] crystallographic axis, revealing variations in both oxygen vacancy concentrations and lattice deformation angle. Oxygen vacancy sites ($V_o$) are marked and highlighted in the corresponding images. High-magnification dDPC micrographs and corresponding atomic structure models, shown in Fig. S4, respectively, clearly resolve all atomic columns, including those associated with oxygen vacancies. Notably, an increase in Hf/Zr lattice distortion is accompanied by a higher density of oxygen vacancies, suggesting a strong correlation between the two. Intriguingly, the oxygen sublattice retains orthorhombic characteristics, alternating between non-polar and polar layers, with oxygen vacancies predominantly located within the asymmetric polar layers (OI-type) of $O_d$-HZO (see also Fig. S5). This observation indicates a significant structural distinction between the $O_d$-phase and the previously reported R-phase of HZO.

*Polarization Activation During the T-to-O Transition.* Similar lattice deformations were also observed in the T-phases (Fig. S6a). Unlike the O phases, in which oxygen columns exhibit distinct crystallographic environments with alternating polar and non-polar layers, the T phase features isotropically coordinated oxygen atoms. As shown in Fig. 2(a), the lattice parameters of the ideal T-phase are consistent with previous reports.[42] In both the pristine T structure and the rhombohedrally distorted T ($T_d$) structure, all oxygen columns remain approximately centered within the surrounding Hf/Zr columns. This configuration implies negligible polarization, in contrast to the ferroelectric behavior typically associated with HZO. To examine the metastability of T-phase nanograins and their contribution to the ferroelectric properties of HZO films, we employed electron-beam illumination in STEM mode.[26,43,44] The electron-beam-induced charging effect generates localized electric fields,[45] which can trigger phase transitions or polarization switching in dielectric materials,[46] while thermal effect and knock-on damage can be ignored (Methods).

HAADF images in Fig. S6b initially show ⟨001⟩-oriented T-phase HZO nanograins exhibiting varying degrees of rhombohedral distortion within the projected rectangle lattice. The corresponding high-magnification dDPC images in Fig. 2(b) reveal the atomic structure of these T-phase grains, in which crystallographically equivalent oxygen columns remain centered within the surrounding cations, consistent with their non-polar character. After several minutes of electron-beam illumination, the ⟨001⟩-oriented T-phase grains transform into [100]-oriented O-phase nanograins, a process occurring beyond the temporal resolution of the present experiment. The resulting O-phase nanograins display a single ferroelectric domain with a polarization vector aligned along the $[001]_o$ crystallographic direction, as confirmed by the atomic-resolution micrographs in Fig. 2(b). This observation suggests a feasible polarization "wake-up" process in the T phase under applied electrical fields, consistent with previous studies.[42,47]

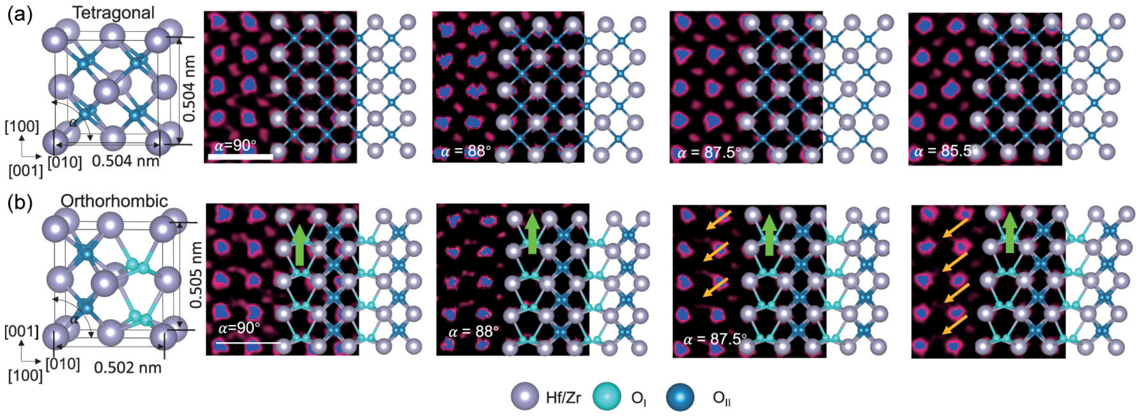

**Fig. 2.** Polarization wake-up in tetragonal (T) and rhombohedrally distorted tetragonal ($\mathrm{T_d}$) HZO. (a) Atomic structure model and high-magnification dDPC images of pristine T-phase HZO nanograins viewed along the [001] zone axis, highlighting the non-ferroelectric tetragonal structure. Scale bar: 0.5 nm. (b) Atomic structural model and corresponding magnified dDPC images of the same domains after prolonged electron-beam exposure, showing polarization aligned along the [001] crystallographic direction and indicating oxygen vacancy sites within the distorted nanograins. Scale bar: 0.5 nm.

During this transition, the oxygen columns differentiate into two distinct types, while the Hf/Zr planes undergo slight shifts to accommodate expanded spacing within the polarized layers and decreased spacing within the non-polar layers. This configuration produces a striped lattice pattern aligned along the [001] polarization direction, as evidenced by integrated differential phase-contrast (IDPC) micrograph comparisons between the initial and final states (Fig. S7). Notably, this ferroelectric activation occurs in both [001]- and [111]-oriented T-phase nanograins, each undergoing a martensitic displacive phase transition into the polar O structure (Fig. S8). Serial TEM imaging, which offers a higher frame rate than STEM, further confirms that the wake-up process is rapid, occurring on the microsecond timescale and lacking reaction-front boundaries, thereby supporting a displacive transition mechanism (Fig. S9).

Oxygen vacancies, though undetectable in the initial T-phase structures, become apparent within the polar layers of the resulting [100]-oriented $\mathrm{O_d}$ phases. The initial rhombohedral distortion angles observed in $\mathrm{T_d}$-phase nanograins persist and now exhibit a clear dependence on oxygen vacancy concentration, consistent with the behavior of pristine oxygen-deficient $\mathrm{O_d}$ phases. In contrast, O-phase structures transformed from undistorted T-phase grains display an ideal lattice devoid of detectable oxygen vacancies. This strong correlation between oxygen vacancies and rhombohedral deformation of the cation lattice in both T- and O-phase structures rules out the possibility of extrinsic vacancy formation induced by electron-beam radiolysis and instead highlights the remarkable lattice adaptability of this binary system in governing its complex polymorphism. Furthermore, the uniform lattice distortion may be associated with a homogeneous distribution of Jahn–Teller centers arising from uniform $\mathrm{Zr^{4+}}$ doping in conjunction with oxygen vacancies. This interaction splits the degenerate d orbitals,[6,48,49] thereby lowering lattice symmetry and reducing the system energy.

The lattice transitions from stoichiometric T-phase and off-stoichiometric $\mathrm{T_d}$-phase into the polar O- or $\mathrm{O_d}$-phase proceed via a martensitic displacive mechanism. These observations reveal the metastable relationship between the T and O phases, largely independent of oxygen vacancy presence, and emphasize the necessity of a "wake-up" process to attain a polar state in T-phase HZO.

*Polarization Switching in the O and $\mathrm{O_d}$ Phase HZO.* The O-phases in HZO thin films, whether pristine or formed via spontaneous transition from the T-to-O phase, exhibit instantaneous polarization switching under electron-beam illumination and the associated electric field. This behavior is captured in atomic-resolution in-situ dDPC micrographs (Fig. 3). Polarization switching induced by the transmitted electron beam can be categorized into three categories based on the initial state of the O-phase nanograins (Fig. S10): (i) a transition from a ferroelectric state to an incomplete antiferroelectric state in fully stoichiometric O-phase HZO observed along the [100] crystallographic direction [Fig. 3(a)]; (ii) a transition from a ferroelectric to a fully antiferroelectric state in oxygen off-stoichiometric $\mathrm{O_d}$-phase viewed along the [100] direction [Fig. 3(b)]; and (iii) a 90° domain reorientation from in-plane to out-of-plane polarization in nanograins containing both out-of-plane polarized, off-stoichiometric [001]-oriented $\mathrm{O_d}$ domains and in-plane-polarized, oxygen-deficient [100]-oriented $\mathrm{O_d}$ domains [Figs. 3(c)–3(e)].

Given that the electric field associated with the illuminating electron beam is oriented out-of-plane, the in-plane polarization is expected to diminish in favor of out-of-plane polarization, consistent with our observations. *In situ* results [Figs. 3(a) and 3(b)] indicate that this reduction in in-plane polarization primarily proceeds through the cell-by-cell emergence of anti-ferroelectric ordering. Initially, the [100]-oriented O-phases exhibit uniform polarization along the [001] direction, with threefold-coordinated OI-type oxygen atoms displaced from the cation center along [001]. Subsequently, in alternating unit cells, these OI-type oxygen atoms shift to a non-centrosymmetric position, symmetrically opposite to the initial site, thereby

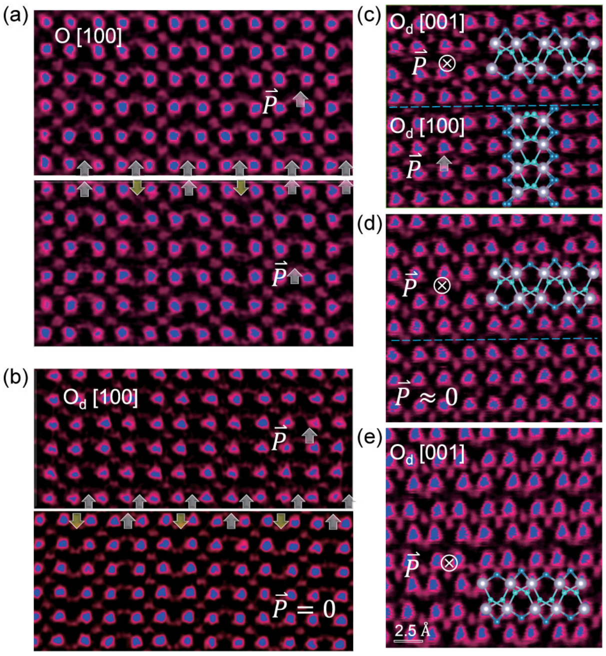

**Fig. 3.** Polarization switching in O and O$_d$ HZO. (a) dDPC images comparing the pristine and final states of the same [100] zone axis-oriented O-phase HZO region under electron-beam illumination, illustrating polarization switching within two unit cells via oxygen displacement. Arrows indicate the polarization direction of individual cells. (b) dDPC images comparing the pristine and final states of [100] zone-axis-oriented distorted O$_d$-phase HZO under the transmitted electric field, revealing polarization switching in half cells via oxygen displacement, characteristic of an antiferroelectric configuration. Arrows denote polarization directions. (c)–(e) dDPC images comparing the pristine and final states of an O$_d$ HZO containing a 90° domain wall between [001]- and [100]-oriented domains. The in-plane polarized [100] domain recedes plane by plane, while the out-of-plane polarized [001] domain expands with the advancing domain wall, ultimately forming a single out-of-plane polarized domain aligned with the electric field. Domain walls are marked by dashed lines.

triggering polarization flipping. This process generates an alternating up–down polarization pattern across portions of the O-phase lattice [Fig. 3(a)] and throughout the entire O$_d$-phase lattice [Fig. 3(b)], characteristic of an antiferroelectric state. Such an oxygen-shift-driven displacive transition is consistent with prior theoretical findings of scale-free, cell-by-cell polarization flipping.[9]

Intriguingly, in nanograin containing a 90° domain wall between [001]-oriented and [100]-oriented O$_d$ phases, the reduction of in-plane polarization within the [100]-oriented O$_d$ domain exhibits a distinct behavior. The OI-type oxygen atoms within the ferroelectric layers [Fig. 3(c)] progressively adopt in-plane non-polar configurations as the domain boundary advances during the growth of the [001]-oriented O$_d$ domain [Fig. 3(d)]. This process ultimately facilitates a transition to out-of-plane polarization [Fig. 3(e)], revealing a domain-wall-mediated nucleation-and-growth switching mechanism akin to the nucleation-limited switching behavior reported in Y-doped $HfO_2$ thin films.[17,50]

The transition from ferroelectric to antiferroelectric ordering involves only a cell-by-cell shift of OI-type oxygen atoms within the Hf/Zr lattice, whereas 90° domain flipping requires nucleation followed by growth through progressive lattice rearrangement. This dependence on the initial structural state, together with the coexistence of two distinct switching pathways, highlights the versatile lattice dynamics of $Hf_{0.5}Zr_{0.5}O_{2-x}$ in enabling robust ferroelectric behavior. Notably, the O$_d$-phase exhibits significantly higher switching efficiency than the ideal O-phase lattice, suggesting fundamentally different lattice dynamics during polarization switching.

*Lattice Dynamics Competitions in O-phase HZO.* Further observations of polarization switching processes indicate that oxygen vacancies, coupled with cation-lattice deformation, stabilize the polar O$_d$ state and elevate the kinetic energy barrier against the thermodynamically favored transition to the monoclinic phase. This effect is evidenced by the partial conversion of stoichiometric O-phase HZO into the M-phase, a transformation that is absent in O$_d$-phases. As shown in Fig. 4, under comparable electron-beam illumination conditions, the [100]-oriented O phase [Fig. 4(a)] does not exhibit oxygen shifting associated with polarization switching; instead, it undergoes layer-by-layer gliding of Hf/Zr planes along the polarization direction [Figs. 4(b)–4(e)]. This process induces a partial transformation from [100]-oriented O-phase (010) planes to [010]-oriented M-phase (100) planes, resulting in a non-polar M-phase structure. Detailed analysis of the dynamic evolution shows that the O-M phase transition proceeds through the propagation of a coherent O/M boundary (Figs. S11 and S12). These observations highlight a detrimental competitive interplay between polar-to-non-polar structural transformation and oxygen-sublattice switching in stoichiometric O-phase HZO, which may contribute to ferroelectric fatigue during device operation. Furthermore, the metastable nature of the stoichiometric O-phase relative to the M-phase is confirmed by the absence of any reverse M-phase transition throughout the experiment.

In stark contrast, the oxygen-deficient O$_d$-phase strongly favors polar switching over transition into the thermodynamically stable, non-ferroelectric M phase. The kinetically stabilized ferroelectric lattice of off-stoichiometric O$_p$-phases HZO highlights the advantages of its low-symmetry, distorted structure, which resists the symmetry-driven transition from the high-symmetry O-phase to the low-symmetry M-phase observed in stoichiometric O-phases. This resistance may explain the persistence of ferroelectricity in HZO at reduced dimensions, overcoming the surface-energy-driven size limitations commonly observed in conventional perovskite ferroelectrics, where small-scale systems tend to favor the high-symmetry paraelectric (cubic) phase over the low-symmetry ferroelectric phase (tetragonal).[51] The robust polar switching and efficient polarization activation observed in nanoscale, oxygen-off-stoichiometric, fluorite-structured binary oxides provide valuable insights for enhancing the performance and reliability of HZO-based devices.

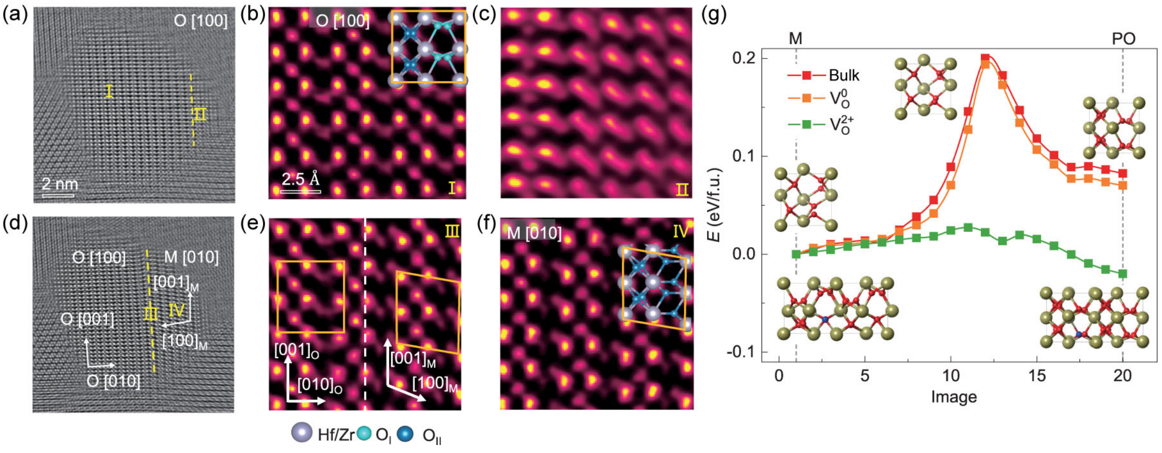

**Fig. 4.** Competing lattice dynamics in O-phase HZO. (a)–(c) IDPC images of an O-[100]-oriented nanograin, showing lattice defect formation near the edge under electron-beam illumination. (d)–(f) IDPC images of the final state corresponding to the region in (a), revealing the emergence of a monoclinic structure at the edge through sliding of Hf/Zr planes, indicative of polarization fatigue. (g) Minimum-energy pathway for the structural phase transition from the nonpolar monoclinic (M) phase to the polar orthorhombic (PO) phase. Insets display atomic configurations along the minimum-energy pathway, where the yellow, red, and blue spheres represent Hf, O, and oxygen vacancy ($V_O$), respectively.

To clarify the role of oxygen vacancies in phase transition, we performed DFT calculations (Methods). The effect of oxygen vacancies was examined by modeling a single vacancy within a $2 \times 2 \times 1$ supercell, corresponding to a vacancy concentration of 3.125% [Fig. 4(g)]. While neutral oxygen vacancies exert only a minor influence on the phase transition energy barriers, charged oxygen vacancies markedly reduce the energy barrier for the M→PO phase transition, decreasing it from 0.20 to 0.03 eV/f.u, in agreement with previous reports.[42] Furthermore, the O phase containing charged oxygen vacancies becomes more stable compared to the non-ferroelectric M phase, consistent with our experimental observations. These results indicate that charged oxygen vacancies play a critical role in stabilizing the polar O phase. It should also be noted that the relative stability of various phases in HZO is effectively modulated by mechanical strain.[52] In our experiments, freestanding films exhibit a greater tendency toward phase transitions compared with electrode-clamped films, as mechanical constraint from electrode structures can elevate the energy barrier for transformation from the $O_d$-phase to the monoclinic (M) phase, thereby enhancing its stability. Further studies, particularly involving in situ biasing experiments within well-defined constrained heterostructures, are essential to elucidate these effects and represent a promising direction for future research.

Compelling evidence thus supports the role of oxygen vacancies in enhancing ferroelectricity in $HfO_2$-based thin films. Atomic-scale mapping of polymorphic transition pathways demonstrates that oxygen vacancies, in conjunction with lattice distortions, kinetically constrain cationic lattice dynamics and stabilize polar HZO, consistent with the DFT results. These findings provide a foundation for the rational structural design and optimization of HZO-based ferroelectric devices.

*Competing Interests.* The authors declare that they have no competing interests.

*Data and Materials Availability.* All data are available in the main text or the supplementary materials.

*Acknowledgements.* This work was supported by the National Natural Science Foundation of China (Grant Nos. 12334001, 52461160301, 52322311, 52427802, 12222414), the National Key R&D Program of China (Grant Nos. 2024YFA1208201, 2021YFA1400500, 2021YFA1400204), and the Youth Innovation Promotion Association of the CAS (Grant Nos. Y2022003 and 2020009).

## References

[1] Böscke T S, Müller J, Bräuhaus D, Schröder U, and Böttger U 2011 *Appl. Phys. Lett.* **99** 102903

[2] Scott J F 2007 *Science* **315** 954

[3] Liu J, Zha J, Yang Y, Lu X, Hu X, Yan S, Wu Z, and Huang F 2024 *Chin. Phys. Lett.* **41** 077701

[4] Ma J Y, Huang Y L, Zhou H J, Wang Y Y, Li J G, Yu X Q, Li H, and Li Y 2024 *Chin. Phys. Lett.* **41** 078202

[5] Lu Y, Zhang D, and Chang K 2025 *Chin. Phys. Lett.* **42** 057402

[6] Cheema S S, Kwon D, Shanker N, dos Reis R, Hsu S L, Xiao J, Zhang H, Wagner R, Datar A, McCarter M R, Serrao C R, Yadav A K, Karbasian G, Hsu C H, Tan A J, Wang L C, Thakare V, Zhang X, Mehta A, Karapetrova E, Chopdekar R V, Shafer P, Arenholz E, Hu C, Proksch R, Ramesh R, Ciston J, and Salahuddin S 2020 *Nature* **580** 478

[7] Luo Q, Cheng Y, Yang J, Cao R, Ma H, Yang Y, Huang R, Wei W, Zheng Y, Gong T, Yu J, Xu X, Yuan P, Li X, Tai L, Yu H, Shang D, Liu Q, Yu B, Ren Q, Lv H, and Liu M 2020 *Nat. Commun.* **11** 1391

[8] Wang Y, Tao L, Guzman R, Luo Q, Zhou W, Yang Y, Wei Y, Liu Y, Jiang P, Chen Y, Lv S, Ding Y, Wei W, Gong T, Wang Y, Liu Q, Du S, and Liu M 2023 *Science* **381** 558

[9] Lee H J, Lee M, Lee K, Jo J, Yang H, Kim Y, Chae S C, Waghmare U, and Lee J H 2020 *Science* **369** 1343

[10] Nukala P, Ahmadi M, Wei Y, Graaf S D, Stylianidis E, Chakrabortty T, Matzen S, Zandbergen H W, Björling A, Mannix D, Carbone D, Kooi B, and Noheda B 2021 *Science* **372** 630

[11] Sang X, Grimley E D, Schenk T, Schroeder U, and LeBeau J M 2015 *Appl. Phys. Lett.* **106** 162905

[12] Schroeder U, Park M H, Mikolajick T, and Hwang C S 2022 *Nat. Rev. Mater.* **7** 653

[13] Yun Y, Buragohain P, Li M, Ahmadi Z, Zhang Y, Li X, Wang H, Li J, Lu P, Tao L, Wang H, Shield J E, Tsymbal E Y, Gruverman A, and Xu X 2022 *Nat. Mater.* **21** 903

[14] Zhou S, Zhang J, and Rappe A M 2022 *Sci. Adv.* **8** eadd5953

[15] Shi S, Cao T, Xi H, Niu J, Jing X, Su H, Yu X, Yang P, Wu Y, Yan X, Tian H, Tsymbal E Y, and Chen J 2024 *Phys. Rev. Lett.* **133** 036202

[16] Shi S, Xi H, Cao T, Lin W, Liu Z, Niu J, Lan D, Zhou C, Cao J, Su H, Zhao T, Yang P, Zhu Y, Yan X, Tsymbal E Y, Tian H, and Chen J 2023 *Nat. Commun.* **14** 1780

[17] Xu X, Huang F T, Qi Y, Singh S, Rabe K M, Obeysekera D, Yang J, Chu M W, and Cheong S W 2021 *Nat. Mater.* **20** 826

[18] Cheng Y, Gao Z, Ye K H, Park H W, Zheng Y, Zheng Y, Gao J, Park M H, Choi J H, Xue K H, Hwang C S, and Lyu H 2022 *Nat. Commun.* **13** 645

[19] Pešić M, Fengler F P G, Larcher L, Padovani A, Schenk T, Grimley E D, Sang X, LeBeau J M, Slesazeck S, Schroeder U, and Mikolajick T 2016 *Adv. Funct. Mater.* **26** 4601

[20] Grimley E D, Schenk T, Sang X, Pešić M, Schroeder U, Mikolajick T, and LeBeau J M 2016 *Adv. Electron. Mater.* **2** 1600173

[21] Feng Z, Wu J, Yang W, Li W, Feng G, Zhu Q, Meng X, Guo X, Tian B, Chu J, and Duan C 2025 *Chin. Phys. Lett.* **42** 056302

[22] Chen H, Zhou D, Xu Y, and Li Q 2025 *Chin. Phys. Lett.* **42** 067301

[23] Wu Y, Zhang Y, Jiang J, Jiang L, Tang M, Zhou Y, Liao M, Yang Q, and Tsymbal E Y 2023 *Phys. Rev. Lett.* **131** 226802

[24] Calderon S, Hayden J, Baksa S M, Tzou W, Trolier-McKinstry S, Dabo I, Maria J P, and Dickey E C 2023 *Science* **380** 1034

[25] Lazić I, Bosch E G T, and Lazar S 2016 *Ultramicroscopy* **160** 265

[26] Zhu L, Jin X, Zhang Y Y, Du S, Liu L, Rajh T, Xu Z, Wang W, Bai X, Wen J, and Wang L 2020 *Phys. Rev. Lett.* **124** 056002

[27] Wang L 2023 *Chin. Phys. Lett.* **40** 050503

[28] Lin T, Gao A, Tang Z, Lin W, Sun M, Zhang Q, Wang X, Guo E J, and Gu L 2024 *Chin. Phys. Lett.* **41** 047701

[29] Wang L, Chen J, Cox S J, Liu L, Sosso G C, Li N, Gao P, Michaelides A, Wang E, and Bai X 2021 *Phys. Rev. Lett.* **126** 136001

[30] Huang X, Wang L, Liu K, Liao L, Sun H, Wang J, Tian X, Xu Z, Wang W, Liu L, Jiang Y, Chen J, Wang E, and Bai X 2023 *Nature* **617** 86

[31] Sun H, Yang Q, Wang J, Ding M, Cheng M, Liao L, Cai C, Chen Z, Huang X, Wang Z, Xu Z, Wang W, Liu K, Liu L, Bai X, Chen J, Meng S, and Wang L 2024 *Nat. Commun.* **15** 9476

[32] Liao L, Yang Q, Cai C, Zhou Y, Sun H, Huang X, Chen P, Wang J, Li X, Tian X, Meng S, Bai X, and Wang L 2024 *Acta Mater.* **273** 119986

[33] Calderon S, Funni S D, and Dickey E C 2022 *Microsc. Microanal.* **28** 2047

[34] Zhong H, Li M, Zhang Q, Yang L, He R, Liu F, Liu Z, Li G, Sun Q, Xie D, Meng F, Li Q, He M, Guo E J, Wang C, Zhong Z, Wang X, Gu L, Yang G, Jin K, Gao P, and Ge C 2022 *Adv. Mater.* **34** 2109889

[35] Hyuk Park M, Joon Kim H, Jin Kim Y, Lee W, Moon T, and Seong Hwang C 2013 *Appl. Phys. Lett.* **102** 242905

[36] Wei Y, Nukala P, Salverda M, Matzen S, Zhao H J, Momand J, Everhardt A S, Agnus G, Blake G R, Lecoeur P, Kooi B J, Íñiguez J, Dkhil B, and Noheda B 2018 *Nat. Mater.* **17** 1095

[37] Qi Y, Singh S, Lau C, Huang F T, Xu X, Walker F J, Ahn C H, Cheong S W, and Rabe K M 2020 *Phys. Rev. Lett.* **125** 257603

[38] Geng W R, Wang Y J, Zhu Y L, Zhang S, Ma H, Tang Y L, Tuo S, and Ma X L 2025 *Nat. Commun.* **16** 8842

[39] Kang S, Jang W S, Morozovska A N, Kwon O, Jin Y, Kim Y H, Bae H, Wang C, Yang S H, Belianinov A, Randolph S, Eliseev E A, Collins L, Park Y, Jo S, Jung M H, Go K J, Cho H W, Choi S Y, Jang J H, Kim S, Jeong H Y, Lee J, Ovchinnikova O S, Heo J, Kalinin S V, Kim Y M, and Kim Y 2022 *Science* **376** 731

[40] Mizoguchi T, Saitoh M, and Ikuhara Y 2009 *J. Phys.: Condens. Matter* **21** 104212

[41] Stemmer S, Chen Z Q, Zhu W J, and Ma T P 2003 *J. Microsc.* **210** 74

[42] Ma L Y and Liu S 2023 *Phys. Rev. Lett.* **130** 096801

[43] Li X, Liu Z, Gao A, Zhang Q, Zhong H, Meng F, Lin T, Wang S, Su D, Jin K, Ge C, and Gu L 2024 *Nat. Mater.* **23** 1077

[44] Li X, Zhong H, Lin T, Meng F, Gao A, Liu Z, Su D, Jin K, Ge C, Zhang Q, and Gu L 2023 *Adv. Mater.* **35** 2207736

[45] Egerton R 2021 *Microsc. Today* **29** 56

[46] Zhi A, Chen Z, Wang J, Xu H, Miao G, Chen P, Han H, Cai C, Li X, Yu G, Wang W, Wang L, Tian X, and Bai X 2025 *Chin. Phys. Lett.* **42** 070717

[47] Müller J, Böscke T S, Schröder U, Mueller S, Bräuhaus D, Böttger U, Frey L, and Mikolajick T 2012 *Nano Lett.* **12** 4318

[48] Schroeder U, Materano M, Mittmann T, Lomenzo P D, Mikolajick T, and Toriumi A 2019 *Jpn. J. Appl. Phys.* **58** SL0801

[49] Jahn H A and Teller E 1937 *Proc. R. Soc. Lond. A* **161** 220

[50] Buragohain P, Erickson A, Mimura T, Shimizu T, Funakubo H, and Gruverman A 2022 *Adv. Funct. Mater.* **32** 2108876

[51] Merz W J 1950 *Phys. Rev.* **78** 52

[52] Gao R, Liu C, Shi B, Li Y, Luo B, Chen R, Ouyang W, Gao H, Hu S, Wang Y, Li D, and Ren W 2024 *Chin. Phys. Lett.* **41** 087701